Nanoscale terahertz scanning probe microscopy

T. L. Cocker [1], V. Jelic[1], R. Hillenbrand [2,3] and F. A. Hegmann [4]*

[1]Department of Physics and Astronomy, Michigan State University, East Lansing, MI, USA

[2] IKERBASQUE, Basque Foundation for Science, 48011 Bilbao, Spain

[3] CIC nanoGUNE BRTA and Department of Electricity and Electronics, UPV/EHU, 20018 Donostia-San Sebastián, Spain

[4] Department of Physics, University of Alberta, Edmonton, Alberta T6G 2E1, Canada

Terahertz radiation has become an important diagnostic tool in the development of new technologies. However, the diffraction limit prevents terahertz radiation (λ ~ 0.01 - 3 mm) from being focused to the nanometre length scale of modern devices. In response to this challenge, terahertz scanning probe microscopy techniques have been developed based on coupling terahertz radiation to subwavelength probes such as sharp tips. These probes enhance and confine the light, improving the spatial resolution of terahertz experiments by up to six orders of magnitude. In this Review, we survey terahertz scanning probe microscopy techniques achieving spatial resolution on the scale of microns to angstroms, with particular emphasis on their overarching approaches and underlying probing mechanisms. Finally, we forecast the next steps in the field.

*e-mail: cockerty@msu.edu

Introduction

Many elementary excitations in materials are found in the terahertz range of the electromagnetic spectrum (0.1 – 30 THz): terahertz radiation can resonantly probe collective charge, spin, and lattice oscillations in solids, the rotations of small polar molecules, and the structural vibrations of large biomolecules [1-6]. As a result, ultrafast terahertz spectroscopy is being used to forge new understanding of materials for next-generation technologies. It has been applied to track emergent phenomena in quantum materials, including insulator-to-metal phase transitions, charge density waves, and superconductivity [1-3]. It has also been a key tool for evaluating charge carrier dynamics in promising materials for solar energy applications [6,7], such as perovskites [8]. Meanwhile, nonlinear terahertz spectroscopy has also been applied to control material properties on ultrafast timescales [3].

However, in many cases, the poor spatial resolution of terahertz spectroscopy is a major obstacle. Key information can even be lost. For example, nanodomain formation is common during phase transitions, perovskites are often polycrystalline, and modern devices are based on <100-nm-scale structures. All of these nanoscale features are far smaller than the minimum spot diameter that can be achieved by focused terahertz radiation, $\lambda/2$, where the wavelength λ spans 0.01 – 3 mm for the terahertz range. Still, terahertz spectroscopy can probe conductivity on length scales far below the diffraction limit for systems of reduced dimensionality, as local depolarization fields [9], mesoscopic structural confinement of charge carriers [10], and quantum confinement of quasiparticles [2] are all imprinted on the complex-valued optical conductivity at terahertz frequencies. Nevertheless, these terahertz conductivities are averaged over all nanostructures in the diffraction limited focal spot, and material properties often hinge on microscopic inhomogeneities. Variations in behaviour associated with nanoparticle size and shape are manifested as inhomogeneous broadening over the macroscopic distribution of nanoparticles. Subtle effects can be yet more difficult to disentangle. On ultrafast timescales, surface states, defect states and inter-nanoparticle hopping all affect photoinduced carrier population and transport but depend sensitively on specific local details. Thus, the prospect of 'zooming in' to the nanoscale to study single nano-objects with terahertz radiation is highly motivating.

A number of imaging concepts have been developed to extend the spatial resolution of ultrafast terahertz spectroscopy from the diffraction limit (Figure 1, far right) to the key length scales of materials science. Aperture-coupled detectors (Figure 1, second from right), tapered photoconductive probes, laser terahertz emission microscopy

(LTEM), and electro-optic sampling in the terahertz near field achieve few micrometre spatial resolution. However, so far, all terahertz microscopy techniques achieving <100 nm spatial resolution have involved coupling terahertz radiation to sharp metal tips. The terahertz fields at the apex of such a tip are enhanced and confined on the length scale of the apex diameter. This confinement is the basis for scattering-type (originally introduced as apertureless) scanning near-field optical microscopy (s-SNOM) and related techniques, which probe the local frequency-dependent dielectric response of a sample with 10 – 100 nm spatial resolution (Figure 1, second from left), as defined by the apex size.

Field enhancement at a tip apex is also essential for lightwave-driven terahertz scanning tunnelling microscopy (THz-STM). It achieves yet finer, <0.1 nm spatial resolution through the detection of tunnel currents induced by strong terahertz near fields (Figure 1, far left). Unlike terahertz near-field microscopy, THz-STM achieves spectroscopic contrast through the voltage induced by the terahertz probe pulse rather than through its frequency content, and hence is not limited to low energy excitations. The bandwidth of the terahertz pulse is important primarily for imbuing atomically resolved scanning probe microscopy with ultrafast temporal resolution, which grants unprecedented angstrom-scale access to local dynamics in materials and devices

In this Review, we provide an overview of terahertz scanning probe microscopy with an emphasis on techniques accessing the key, <100 nm length scale of materials science for modern technology. The Review follows the theme of zooming in to the nanoscopic domain with terahertz radiation, as visualized in Figure 1. We begin with a snapshot of terahertz microscopy techniques reaching micron-scale spatial resolution. We then turn our focus to the central concept of coupling terahertz radiation to sharp metal tips, which is common to all terahertz microscopy techniques with <100 nm spatial resolution. Our primary objective is to compare and contrast the probing mechanisms underlying different classes of techniques rather than to comprehensively summarize all experiments performed to date, as such summaries can be found elsewhere [11-14]. We divide tip-based terahertz microscopy schemes into two sections: (i) s-SNOM and related techniques that probe local dielectric properties and (ii) THz-STM, which probes atomic tunnel junctions. The boxes illustrate selected key concepts, whereas the text summarizes exciting recent advances from the literature. Finally, we provide an outlook on the future of nanoscale terahertz scanning probe microscopy.

Scanning near-field terahertz microscopy on the micron scale

The long wavelength of terahertz radiation (e.g. $\lambda = 0.3$ mm for 1 THz) leads to macroscopic terahertz focal spot sizes (Figure 1, far right). Conversely, common techniques for generating and detecting single-cycle terahertz pulses rely on femtosecond near-infrared pulses, and this can be leveraged to achieve spatial resolution on the length scale of the near-infrared focal spot rather than the terahertz focal spot. The terahertz generation version of this concept is LTEM, where a tightly focused beam of near-infrared pulses is scanned over a surface and the emitted terahertz field is detected in reflection geometry [15]. The spatial resolution of LTEM is governed by the focusing conditions of the excitation beam, and few-micron-scale surface features have been imaged [15]. A complementary technique based on terahertz detection is electro-optic sampling in the terahertz near-field [16]. In this case, the terahertz near fields in the vicinity of a subwavelength object induce a birefringence in a nearby electro-optic crystal that is read out by a near-infrared gate pulse [17,18]. The spatial resolution of the technique is defined by the near-infrared imaging conditions (e.g. 5 μm spatial resolution for a 10 × focusing objective [18]). This configuration has also been used for terahertz spectroscopy of subwavelength objects [19], including polarization-dependent measurements of biological samples [20].

Alternatively, in aperture-based scanning terahertz microscopy techniques, the effective terahertz spot size is reduced below the diffraction limited focus directly by detecting radiation that has passed through a subwavelength hole (Figure 1, second from right). Individual apertures with diameter $d < \lambda/100$ can be manufactured in metal surfaces by standard techniques, but utilizing these apertures for subwavelength imaging and spectroscopy requires sophistication, as a single subwavelength hole strongly attenuates incident radiation. The terahertz detector must have extremely high sensitivity and signal-to-noise ratio because the detection limit defines the minimum practical aperture size. A breakthrough has been to employ detectors that are also very thin, i.e. thin enough that they fit within a distance $z < d$ in the direction of light propagation. In this range, the terahertz field profile is made up of both propagating [21] and evanescent components [19,22] and a thin detector can sample a far higher terahertz field. Hence, the aperture can be made significantly smaller. Studies have realized this concept through, e.g., a gallium arsenide quantum well detector [23], a rectifying antenna that relies on either an indium arsenide nanowire or black phosphorus flake as an active element [24], or a photoconductive antenna integrated with a distributed Bragg reflector

[22], with a current record spatial resolution of 3 μm [22]. These developments are currently the chief driver in improving the spatial resolution of aperture-based terahertz microscopy and will be critical for reaching the sub-micron scale.

A key strength of aperture-based terahertz scanning probe microscopy is its polarization sensitivity. Many of the terahertz field detectors integrated into aperture probes naturally discriminate between polarization states [22,24]. This lends itself to vectorial field imaging of samples like the meta-atom resonators that collectively form terahertz metamaterials when grouped into ordered arrays. An alternative but related approach to mapping local terahertz fields with polarization sensitivity is to fabricate a photoconductive terahertz detector on a tapered probe that activates when illuminated by a near-infrared laser pulse. Spatial resolution below 10 μm is achieved by virtue of the small photoconductive gap size [25], while the detectable field direction is defined by the orientation of the detector [26]. By individually scanning each photoconductive probe over a sample to gather the spatial distribution of the field in the corresponding direction, a three-dimensional map of the local terahertz field magnitude and direction can be constructed [26]. Looking forward, the polarization sensitivity of the techniques described in this section gives them an advantage over tip-based approaches for certain applications, ensuring their continued importance despite comparatively coarse spatial resolution.

Scattering-type scanning near-field terahertz microscopy

Scattering-type scanning near-field optical microscopy is based on the central concept of illuminating a sharp scanning probe tip and recording the scattered light as a function of tip position [11-14,27-33]. This concept can be applied across a broad range of illumination frequencies. For s-SNOM at terahertz frequencies [34-38], terahertz fields are enhanced and confined at the tip apex due to the lightning rod [38] and antenna [35,39] effects, resulting in a nanofocus. The nanofocus consists of evanescent fields that decay into free space on the length scale of the tip-apex radius of curvature (10 – 100 nm), as confirmed by electromagnetic simulations (Fig. 2a, ref. [38]). When the tip is in close proximity to a sample, the nanofocused fields are scattered through the tip-sample near-field interaction, enabling optical nanoimaging at terahertz frequencies.

Modern s-SNOM is based on atomic force microscopy (AFM), where standard, metalized cantilever AFM tips simultaneously serve as both topographic and near-field scattering probes. A parabolic mirror can be conveniently used to both focus light onto the tip and collect scattered radiation. However, AFM tips are typically shorter than 20 μm, and thus do not couple efficiently to terahertz wavelengths. This has motivated the development of alternative AFM probes. Terahertz s-SNOM signals have been enhanced by adjusting the tip length to match geometric antenna resonances [39-41] or by increasing the apex diameter [40]. Meanwhile, terahertz s-SNOM spatial resolution has been improved through apex sharpening, reaching 13 nm at a metal/dielectric boundary [40]. However, the signal-to-noise ratio decreases for sharper tip apex radii, potentially restricting the sample details that can be captured experimentally. Terahertz s-SNOM imaging therefore benefits from the growing availability of strong, coherent sources of terahertz radiation [5], such as gas lasers [38,40,42], quantum cascade lasers [43], free electron lasers [44,45], and electronics-based terahertz transceivers [46,47].

The evanescent terahertz fields coupled to an s-SNOM tip are polarized normal to the surface of the tip and oriented longitudinally at its apex [16]. When the tip is close to a sample surface, the terahertz near fields interact with (i.e. reflect off) the sample and act back on the tip, inducing an additional tip polarization [11,30,31,40]. The induced polarization can be described by a net dipole that radiates (i.e. scatters) terahertz light into the far field, where it can be detected. The dielectric properties of the sample volume contributing to the near field reflection are imprinted on the scattered terahertz field through the local Fresnel reflection coefficient, as detailed in Box 1. In short, resonances in the dielectric function due to low-energy elementary excitations determine contrast in the scattered terahertz field. For example, the scattering efficiency increases for decreasing illumination frequency directly below a plasmonic resonance [32,38] (as is the case for far-field reflection). Consequently, nanoscale variations in free carrier density can be visualized by continuous wave terahertz s-SNOM, as has been demonstrated for a transistor chip (Fig. 2b) with 40 nm spatial resolution [38]. On the other hand, terahertz s-SNOM contrast can also be affected by larger scale structures, such as connections to a ground plane, without impacting the spatial resolution [47]. These effects therefore have to be considered when interpreting and analyzing local terahertz contrasts.

A key ingredient for s-SNOM at all illumination frequencies is efficient background suppression, i.e. the ability to record the tip-scattered field that is generated exclusively by the near-field interaction between the tip and sample.

153 This is most commonly done by oscillating the tip at a frequency Ω (e.g. by operating the AFM in tapping mode)
154 and detecting the scattered light at a higher harmonic (demodulation) frequency of Ω [31,32], as outlined in Box 1.
155 A critical aspect of this approach is that the far-field detector should be sensitive to electric field to avoid ambiguity
156 in optical contrast [31,48], since measurements that record only intensity at nΩ inadvertently mix tip-scattered near
157 and far fields. Interferometric mixing schemes using a reference field that is larger than the signal (or modulated) can
158 grant an intensity detector access to the relative optical phase in addition to the spectral amplitude; hence, this
159 approach has been employed for terahertz s-SNOM in conjunction with narrowband [38,40,42,43] and broadband
160 [49,50] sources. Meanwhile, for s-SNOM experiments with pulsed illumination, terahertz technology holds a distinct
161 advantage over the common detection techniques of other frequency ranges: the oscillating electric fields of phase-
162 stable terahertz pulses are routinely detected directly by electro-optic or photoconductive sampling [1-6]. This
163 provides, simultaneously, both the spectral amplitude and absolute phase of the terahertz pulse. In s-SNOM
164 experiments employing higher harmonic signal demodulation, recording the peak of a scattered near-field terahertz
165 transient as a function of tip position reveals the local dielectric properties of the sample integrated over the terahertz
166 pulse bandwidth [51-55]. For example, broadband, field-resolved terahertz s-SNOM images of vanadium dioxide
167 [52] show local increases to the free carrier conductivity as the sample is heated across the insulator-to-metal phase
168 transition temperature (Fig. 2c, ref. [52]).

169 Alternatively, the entire terahertz near-field waveform can be recorded at a particular tip position to perform
170 spectroscopy with <100 nm spatial resolution [37,53], or waveforms can even be recorded as a function of tip position
171 to perform hyperspectral nano-imaging [51,54,55]. In the far-field analogue of nano-spectroscopy, i.e. terahertz time-
172 domain spectroscopy (THz-TDS), the Fourier transforms of reference and sample waveforms are compared to extract
173 the real and imaginary components of the sample's complex permittivity (or, equivalently, complex conductivity or
174 index of refraction) through the Fresnel equations without using the Kramers-Kronig relations [1-6]. Field-resolved
175 nano-spectroscopy is similarly sensitive to the complex permittivity, but the procedure for extracting it is more
176 complicated due to the presence of the tip. Nevertheless, by modelling the tip-sample near-field interaction (see Box
177 1) it is possible to obtain the spatially dependent complex terahertz permittivity with nanoscale resolution, as has
178 been demonstrated for hyperspectral imaging of crystalline lactose in polyethylene (Fig. 2d-f, ref. [55]). The lactose

features molecular resonances in the terahertz range, which can be identified in the local dielectric function and attributed to distinct lactose sterio isomers with precise molar sensitivity [55].

Establishing time-resolved terahertz spectroscopy (TRTS) on the nanoscale remains a work in progress, but pump-probe nano-spectroscopy has been established for mid-infrared (multi-terahertz) pulses [56, 57], including field-resolved experiments achieving sub-cycle time resolution via ultrabroadband electro-optic sampling [56]. At terahertz illumination frequencies, first pump-probe experiments have also been demonstrated, e.g. tracking the peak of the scattered terahertz near field as a function of optical-pump / terahertz-probe delay [58]. Further advances in this area are anticipated for the near future. Other new experimental developments, such as cryogenic s-SNOM [59-61], open the door to terahertz nano-spectroscopy of increasingly diverse phenomena, including terahertz resonances that are not observable at room temperature, where the thermal energy is large compared to the terahertz photon energy ($h\upsilon/k_B$ = 48 K for υ = 1 THz).

In addition to standard terahertz s-SNOM, where the tip is illuminated by terahertz radiation and light scattered from the tip apex is detected in the far field, alternate experimental modalities have been developed that extend the reach of tip-based terahertz near-field microscopy yet further. For example, a terahertz single-photon counter enables an approach that does not require input radiation (Fig. 3a,b, ref. 62). Instead, the tip outcouples the thermal fluctuations of the sample, thereby probing the sample's local photonic density of states [62-64]. A recent cryogenic implementation of passive terahertz s-SNOM [65] promises to improve the signal-to-noise ratio, acquisition speed, and versatility of the technique.

Another possibility enabled by s-SNOM is polariton mapping. The near fields at the sharp apex of the s-SNOM tip possess a broad momentum distribution, allowing them to excite polaritons that propagate radially away from the tip apex. The polaritons reflect off sample edges and create interference patterns that can be visualized by scanning the tip position and recording the scattered near field. This concept was first demonstrated at mid-infrared frequencies [66,67], but has also been applied to terahertz s-SNOM [68]. A further adaptation at terahertz frequencies has been to read out plasmon interference via a photocurrent generated in a graphene device [39,69,70]. In this way, acoustic terahertz plasmons have been revealed in graphene (Fig. 3c,d, ref. 69) with high signal-to-

204 noise ratio. Terahertz polariton mapping may find future prominence in the study of exotic new materials,
205 especially those in which polariton lifetimes are longer than a terahertz oscillation cycle.
206 Finally, scanning probe tips have been used to extend LTEM to the nanoscopic domain [71]. In laser terahertz
207 emission nanoscopy (LTEN), an optical or near-infrared pump pulse illuminates the sample and tip (Fig. 3e, ref.
208 [71]). Terahertz radiation is generated by the ultrafast response of the sample surface. The tip acts as a scannable
209 antenna in this configuration, enhancing and outcoupling the local terahertz emission with nanoscale precision
210 [71,72], as shown in Fig. 3f. LTEN not only complements ultrafast pump-probe terahertz s-SNOM, but is also
211 inextricably linked for samples in which photoexcitation leads to terahertz emission [58]. In the future, these
212 experiments may be further correlated with ultrafast AFM, which is sensitive to the femtosecond nonlinear
213 polarization underlying terahertz generation at a surface [73]
214
215 **Lightwave-driven terahertz scanning tunnelling microscopy**
216 The experimental geometry of THz-STM (Fig. 4a, ref. 77) is similar to that of terahertz s-SNOM, but its underlying
217 physical mechanism is different. Whereas terahertz s-SNOM typically probes the linear dielectric response of a
218 sample, THz-STM operates in the strong-field regime [3,78], where the terahertz evanescent fields at the tip apex
219 reach the scale of interatomic fields in solids and coherently control electron tunnel currents between the tip and
220 sample (Fig. 4b, ref. 79), as detailed in Box 2. The THz-STM signals are read out by detecting the rectified component
221 of the lightwave-driven current using conventional STM electronics [77]. This provides a femtosecond probe of the
222 tunnel junction that can be used in pump-probe schemes [77,80-82] for ultrafast STM experiments. Since the terahertz
223 probe behaves as an ultrafast yet quasi-static bias voltage across the tunnel junction it is generally applicable to all
224 STM samples. THz-STM also resolves other longstanding issues of ultrafast STM, such as sample heating [83].
225 A second, related distinction should be made between spectroscopy in THz-STM compared to terahertz s-SNOM.
226 In terahertz s-SNOM, as in THz-TDS, the spectral amplitude of the input defines its interaction with the sample (see
227 Box 1). Conversely, spectroscopy in THz-STM more closely resembles scanning tunnelling spectroscopy (STS, see,
228 e.g., ref. 84), as the instantaneous terahertz field defines the Fermi level alignment between the sample and tip.
229 Sweeping the terahertz peak field is similar to sweeping the voltage in STS (Fig. 4c,d, ref. 79,85). However, the

rectified charge measured by THz-STM is the temporal integral of the oscillating terahertz-induced current, so modelling is necessary to extract the differential conductance sampled by the terahertz pulse [77,79,80,85,86]. Even in unexcited junctions this can differ from the static differential conductance, as has been observed for the silicon 7×7 surface (Fig. 4e, ref. 85). The frequency content of the input terahertz pulse is also relevant for defining the voltage transient across the tunnel junction. Terahertz coupling to the tip and field enhancement at its apex depends on both the tip shape and input spectrum [81,85,87-90]. New tools have been developed for characterizing the electromagnetic waveform at the tip apex in response to this challenge, including terahertz photoemission sampling [81,89,91], measurements on THz-STM reference samples [81], and local field sampling via a single-molecule switch [90].

A third distinction can be made when comparing the spatial resolutions of THz-STM and terahertz s-SNOM. The radius of curvature of the tip apex sets the spatial resolution of terahertz s-SNOM through localization of the evanescent terahertz near fields. In contrast, THz-STM relies on these evanescent fields for enhancement [92,93,94] to reach the strong-field regime, but does not rely on them for its spatial resolution. Instead, the spatial resolution of THz-STM is determined by the tunnel junction, since the detected current must pass through it. This allows atomic resolution to be achieved for THz-STM in ultrahigh vacuum, cryogenic conditions [80,85], as has been shown for silicon (Fig. 4f, ref. 85).

Some of the most exciting experiments enabled by THz-STM are pump-probe measurements with simultaneous extreme temporal and spatial resolutions [77,80-82]. This was demonstrated in the inaugural THz-STM study [77], where near-infrared photoexcitation was shown to modulate the THz-STM response of an indium arsenide nanodot on sub-picosecond timescales (Fig. 4g, ref. 77). These dynamics, which were attributed to transient charging due to different electron and hole trapping times [95], were captured in ultrafast THz-STM snapshot imaging under ambient conditions (Fig. 4h, ref. 77). Near infrared pump / THz-STM probe experiments have also been reported for bulk 2H-$MoTe_2$ and Bi_2Se_3 surfaces [81], where differing behaviour in response to dynamics faster and slower than the terahertz oscillation cycle, respectively, highlights the need for a comprehensive theoretical foundation for time-resolved terahertz STS (THz-STS). In principle, THz-STS has the potential to reveal the transient occupation of the local density of states with atomic resolution if provided a sophisticated framework for data analysis.

Alternatively, lightwave-driven tunnelling can be used as an atomically localized pump in a pump-probe scheme incorporating two terahertz-driven tunnelling processes. This has been shown in single-molecule THz-STM experiments performed at 10 K in ultrahigh vacuum [80], where one terahertz-driven tunnelling event coherently launched the oscillation of the molecule above the substrate [96] and a second read out the motion of the molecule with ultrafast time resolution (Fig. 4i, ref. 80). These experiments further demonstrated orbitally selective terahertz-induced tunnelling with sensitivity better than 1 electron per terahertz pulse, culminating in THz-STM images of the electron density in the highest occupied molecular orbital (Fig. 4j, ref. 80) and lowest unoccupied molecular orbital of pentacene with sub-Angstrom spatial resolution [80]. More recently, THz-STM has been combined with action spectroscopy of single molecules, where a terahertz pump pulse exerted a local force on a magnesium phthalocyanine molecule, inducing a coherent hindered rotation of its frame [82,90]. A subsequent terahertz probe pulse stimulated tunnelling through one of the molecular orbitals, thereby destabilizing the molecule's adsorption position on the substrate, which rests in on one of two orientations when unexcited. By reading out the orientation of the molecular switch after each terahertz-induced tunnelling event, the terahertz-pump-induced hindered rotation of the molecule was shown to affect its switching probability [82].

Outlook

Terahertz scanning probe microscopy has been marked by a series of recent technical breakthroughs. These advances enable tip-based terahertz measurements with simultaneous <100 nm spatial resolution and ultrafast temporal resolution, opening up entirely new avenues for exploration. Terahertz scanning probe microscopy techniques promise new insights into novel nanoscale device architectures, including both those fabricated by top-down or bottom-up synthesis. The local dynamics of low-energy elementary excitations in these devices will soon come into clearer view, as will related phenomena like hot carrier transfer between molecules and nanoantennae. We expect special emphasis will be placed on nanoscale conductivity dynamics relevant to next-generation optoelectronics and solar energy technology [1-7]. Ultrafast terahertz microscopy at low temperatures further promises to elucidate the complex interplay between competing degrees of freedom in correlated electron and topological materials. First experiments have also demonstrated the promise of aperture-based terahertz microscopy [20] and s-SNOM [97] for

investigating biological samples. These capabilities may yet be expanded through the application of complementary terahertz microscopy techniques.

In general, terahertz s-SNOM lays a pathway to recreate the consistent success of ultrafast far-field terahertz spectroscopy – now with nanoscale spatial resolution. Alternate near-field techniques based around the scattering theme, such as those highlighted in the corresponding section above, provide both unique and complementary information to conventional s-SNOM. They may even prove capable of addressing physics that cannot be accessed by other means, though in some cases further development is needed to reveal the full scope of their strengths and weaknesses. Meanwhile, nonlinear s-SNOM is relatively unexplored, but promising [98,99]. Nonlinear terahertz spectroscopy and terahertz coherent control in the far field is an active and growing area of research [3]. Extending these ideas to the nanoscopic domain is the natural next step in many cases. LTEN is one of the first forays in this direction, though it primarily probes the nonlinear dielectric function at near-infrared frequencies rather than terahertz frequencies.

Interestingly, THz-STM can be thought of as a form of extremely nonlinear near-field microscopy (albeit one specific to conducting substates) since it operates in the strong-field regime of light-matter interactions. Already THz-STM provides exclusive access toultrafast dynamics in single molecules and nanostructures with atomic resolution [80,82,85,90], while theoretical studies have proposed THz-STM experiments to capture transient wavefunction dynamics within single molecules [100,101]. We expect these possibilities will be manifested in exciting new developments in upcoming years through an expanding network of researchers entering the field. For example, very recent reports have shown near-infrared pump / THz-STM probe snapshot imaging of electron dynamics in C_{60} multilayer structures [102], terahertz-field-driven scanning luminescence spectroscopy of gold nano-islands on a silver surface [103], and terahertz pump / terahertz probe dynamics in the candidate excitonic insulator Ta_2NiSe_5 using a new variable-repetition-rate laser source for THz-STM [104]. THz-STM is also one of the leading techniques in the emerging discipline of molecular movie making [105], where it competes with large-scale facilities. THz-STM may yet find new strengths through its intrinsically quantum mechanical nature, for example evaluating nanoscale qubit candidates and decoherence mechanisms for quantum information processing [106]. In the other extreme, THz-STM is capable of sensing and controlling not only terahertz-induced tunnelling events composed of

single quanta [80,82,90], but also instantaneous current densities far beyond what is accessible with conventional STM [79,85,86]. Similar physics is being pursued for electron sources to service ultrafast electron microscopy [91,107,108].

Looking forward, we envision the connections between THz-STM and other related techniques moving beyond analogy. THz-STM and terahertz s-SNOM could be combined in a single apparatus capable of spanning linear to nonlinear, and ultimately to strong-field terahertz microscopy. Such an ultimate terahertz microscope might also operate under cryogenic [59-61,80,82,85,90,103-105] and ultrahigh vacuum [80-82,85,89,90,103-105] conditions, though tip engineering will be an important consideration; the demands of each technique must be satisfied while accounting for environmental constraints like reduced damping of the s-SNOM tip oscillation. Extending the temperature range yet further, from liquid helium temperatures [80,82,90] to millikelvin temperatures may prove more challenging due to limited optical access, but would open up further exciting avenues, particularly in quantum information science. Other advanced imaging methods could also be incorporated thanks to the simple and versatile geometry common to terahertz s-SNOM and THz-STM. Finally, integrating lightwave-driven tunneling at higher frequencies would provide further functionality [89,109-111]. Nevertheless, we expect terahertz will prove to be a Goldilocks frequency range for many samples and yield a wealth of new scientific insight on the nanoscale.

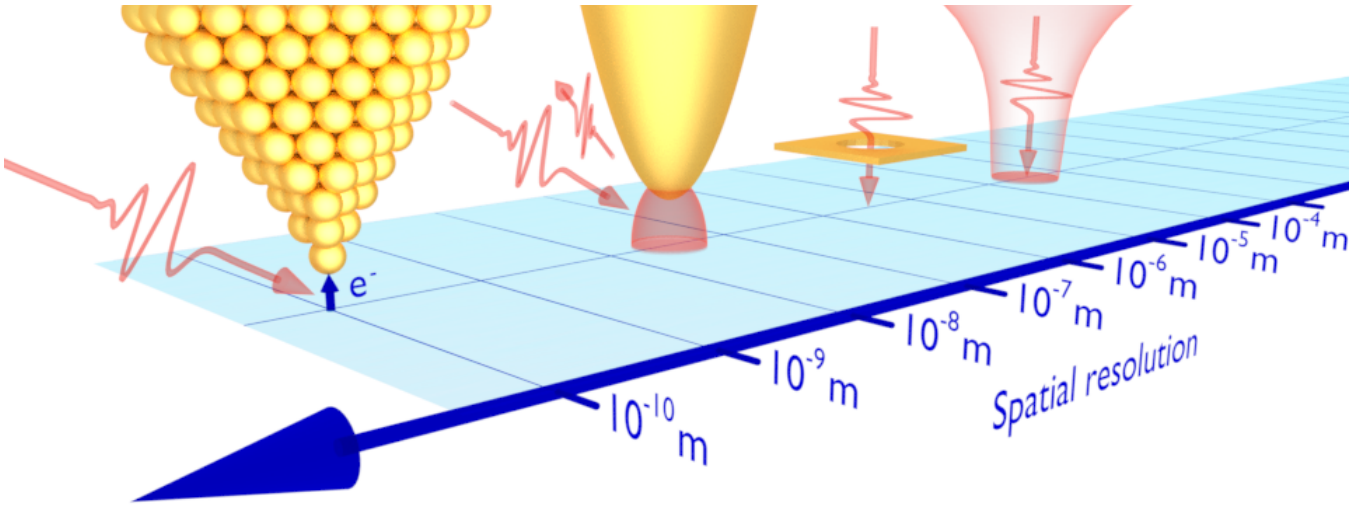

Figure 1 | Zooming in on surfaces with terahertz microscopy. *Free space focusing of a Gaussian beam composed of terahertz pulses with 1 THz centre frequency can reach a minimum focal spot diameter of ~0.15 mm (far right). Aperture-based terahertz near-field techniques can improve the spatial resolution of terahertz imaging to the few micrometer scale (second from right). The spatial resolution can be improved yet further, to the 10 – 100 nm scale, by coupling terahertz pulses to a sharp metal tip and performing terahertz s-SNOM (second from left). Atomic spatial resolution (~0.1 nm) is achieved by lightwave-driven terahertz scanning tunnelling microscopy, where tip-coupled terahertz pulses coherently control the tunnel current between the tip and sample (far left).*

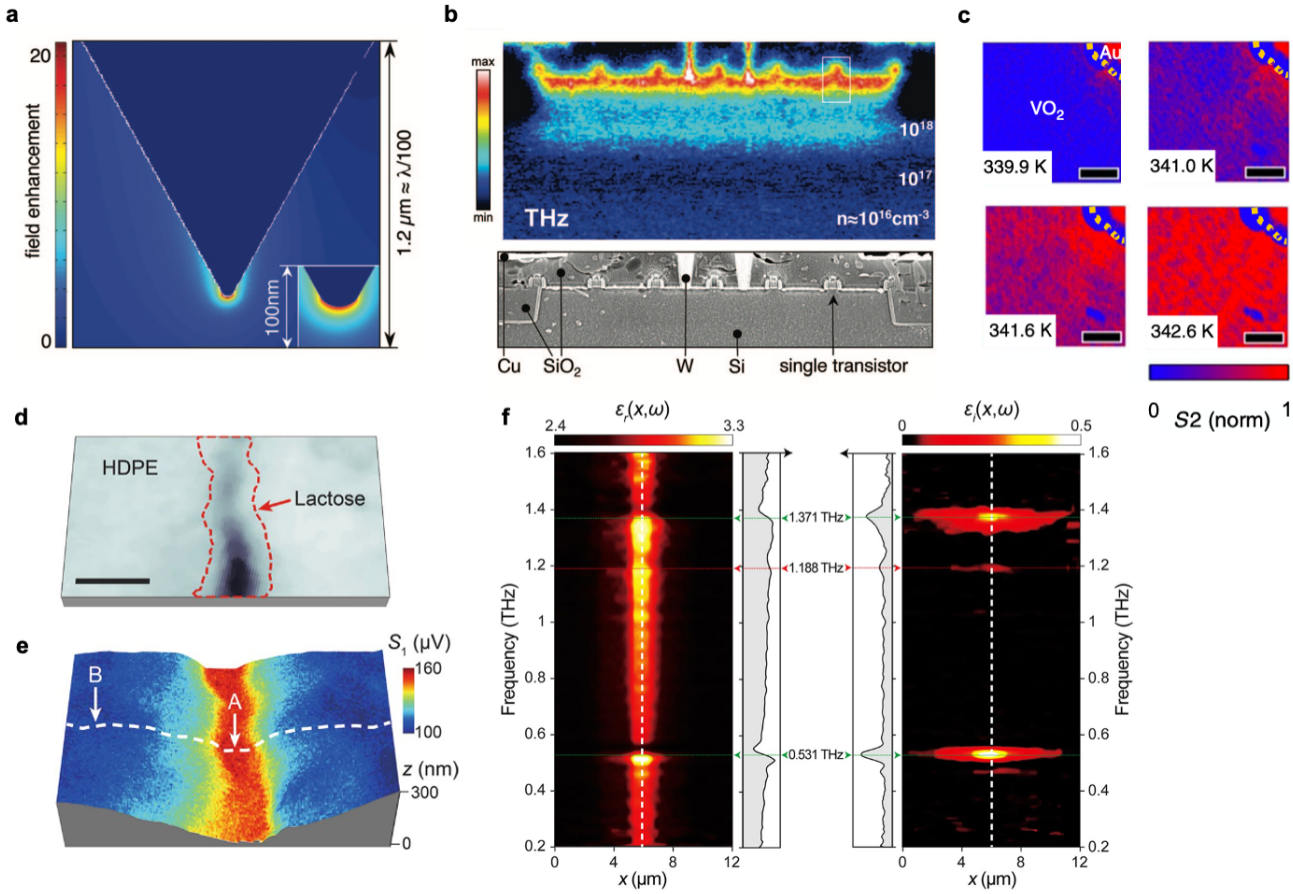
a
field enhancement
20
0
1.2 μm ≈ λ/100
100nm
b
max
min
THz
10^18
10^17
n≈10^16cm^-3
Cu
SiO2
W
Si
single transistor
c
VO2
Au
339.9 K
341.0 K
341.6 K
342.6 K
0
S2 (norm)
1
d
HDPE
Lactose
e
S1 (μV)
160
100
B
A
z (nm)
300
0
f
εr(x,ω)
2.4
3.3
εi(x,ω)
0
0.5
1.371 THz
1.188 THz
0.531 THz
Frequency (THz)
x (μm)

Figure 2* | *Scattering-type scanning near-field terahertz microscopy. ***a****, Terahertz radiation focused onto a sharp metal tip is enhanced and confined at its apex, as demonstrated by numerical electrodynamic calculations.* ***b****, Continuous wave terahertz s-SNOM imaging (top panel) of a transistor chip reveals contrast in the local carrier density, n, with ~40 nm spatial resolution. In the bottom panel, the layout of the transistor chip is detailed in a scanning electron microscope image of a similar (but decoration etched) transistor.* ***a*** *and* ***b*** *are reproduced from [38].* ***c,*** *Broadband terahertz s-SNOM images of vanadium dioxide (VO_2) showing the evolution of the local free carrier conductivity as the sample is heated across its insulator-to-metal phase transition temperature (reproduced from [52]). The distinct metallic puddles observed in paradigmatic mid-infrared s-SNOM experiments of VO_2 [74] are absent at terahertz frequencies, providing key insights about the nature of the phase transition.* ***d****, Terahertz s-SNOM is sensitive to not only free carrier concentration, but also local molecular resonances. This has been demonstrated for crystalline lactose composed of two sterio isomers. An optical microscope image shows the sample pellet, which has been pressed together from lactose and high-density polyethylene (HDPE) powders.* ***e****, Broadband terahertz s-SNOM image of the lactose/HDPE pellet (colour mop) overlaid on the simultaneously recorded atomic force microscope topography. Additionally, terahertz hyperspectral nano-imaging can be performed by recording the amplitude and phase of scattered terahertz pulses as a function of tip position, e.g. along the white dashed line.* ***f****, Spatially dependent complex terahertz permittivity along the white dashed line in* ***e****, extracted using a theoretical model based on the line dipole image method with quasi-static electrostatic boundary conditions. The green lines indicate resonances from the α-lactose anomer and the red line indicates a resonance from the β-lactose anomer.* ***d*** *–* ***f*** *are reproduced from [55].*

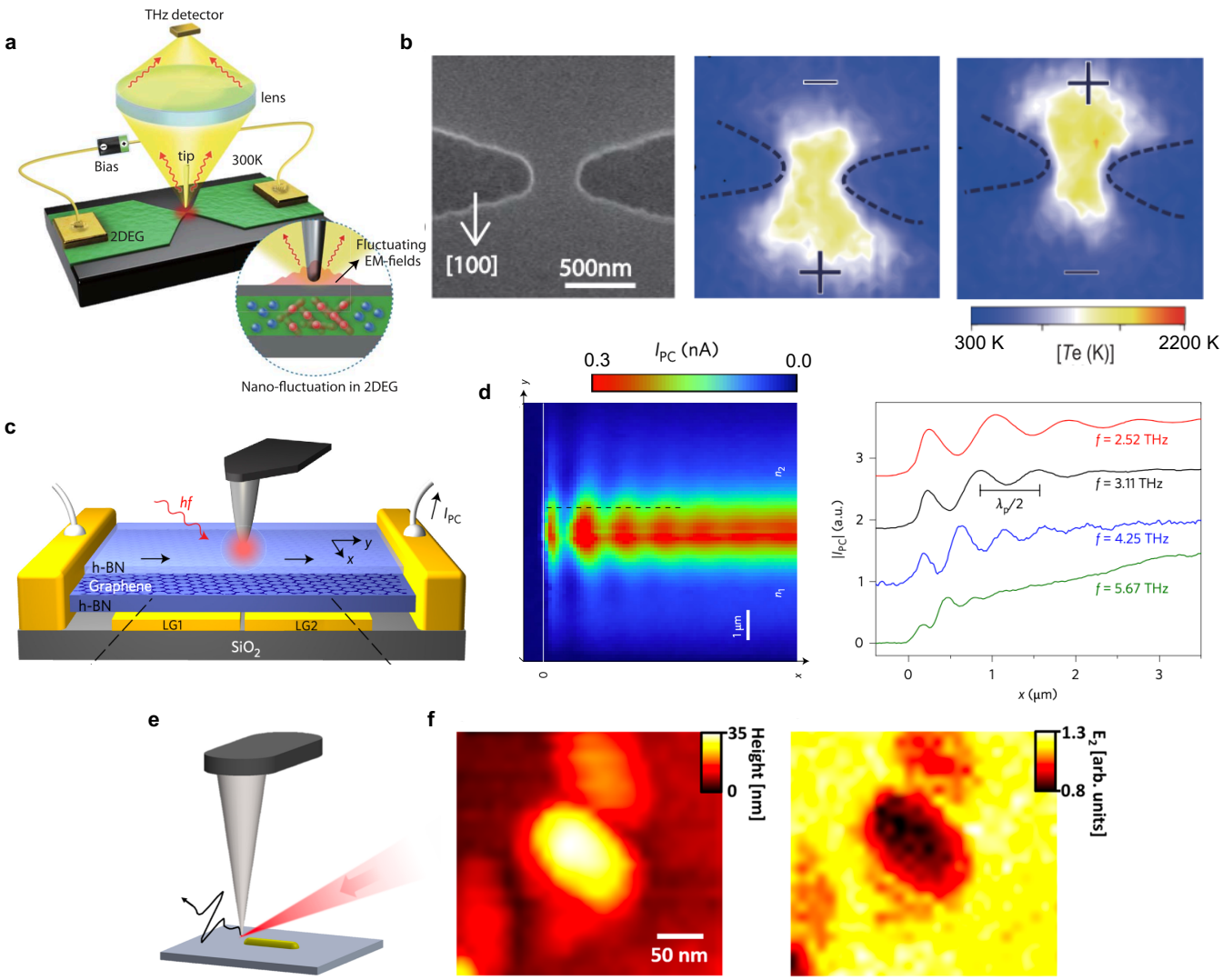
a
THz detector
lens
Bias
tip
300K
2DEG
Fluctuating EM-fields
Nano-fluctuation in 2DEG
b
[100]
500nm
300 K
[Te (K)]
2200 K
c
hf
I_{PC}
y
x
h-BN
Graphene
h-BN
LG1
LG2
SiO_2
d
0.3
I_{PC} (nA)
0.0
y
n_2
n_1
1 μm
0
x
$|I_{PC}|$ (a.u.)
f = 2.52 THz
f = 3.11 THz
$\lambda_p/2$
f = 4.25 THz
f = 5.67 THz
x (μm)
e
f
35
Height [nm]
0
50 nm
1.3
E_z [arb. units]
0.8

Figure 3* | *Alternate tip-based terahertz near-field nanoscopy techniques. ***a****, Scanning near-field terahertz noise microscopy removes the need for a terahertz source in s-SNOM and instead outcouples thermal fluctuations of the sample, detecting the scattered intensity with a charge-sensitive infrared phototransistor detector capable of single-terahertz-photon sensitivity. Operating in contact-free mode prevents the tip from disturbing the sample temperature.* ***b****, Scanning near-field terahertz noise microscopy has been applied to map hot-electron energy dissipation in a nanoconstriction device. Left: scanning electron microscope image of the GaAs/AlGaAs two-dimensional electron gas device. The constriction is in the centre and electrons flow through it along the [100] crystallographic axis in the direction defined by the bias (i.e. top-to-bottom or bottom-to-top in the image). Right: terahertz noise microscopy images of nanoconstriction device. Higher electron temperatures,* T_e*, on the 'downstream' side of the nanoconstriction were attributed to carrier heating.* ***a*** *and* ***b*** *are reproduced from [62].* ***c****, Terahertz radiation coupled to an s-SNOM tip can launch surface plasmon polaritons on graphene thanks to the broad distribution of momentum vectors present at the tip apex [75]. When the tip is positioned near the graphene edges, polariton interference occurs. This can be read out via the photocurrent,* I_{PC}*, in a transistor geometry.* ***d****, Raster scanning the tip parallel (y) and perpendicular (x) to the edge of a graphene sample in such a geometry reveals surface plasmon polariton interference in regions of optimal carrier doping (left). The plasmon wavelength changes with terahertz input frequency (right) providing a means to map out the dispersion of the propagating surface-bound mode – in this case, highly-localized acoustic plasmons.* ***c*** *and* ***d*** *are reproduced from [69].* ***e****, In laser terahertz emission nanoscopy, ultrafast near-infrared pulses are focused onto a sample, generating terahertz pulses at its surface that are locally outcoupled by the s-SNOM tip.* ***f****, In the first demonstration of the technique, contrast was shown between gold nanorods and an InAs substrate Left: topography; right: peak scattered terahertz electric field.* ***e*** *and* ***f*** *are reproduced from [71].*

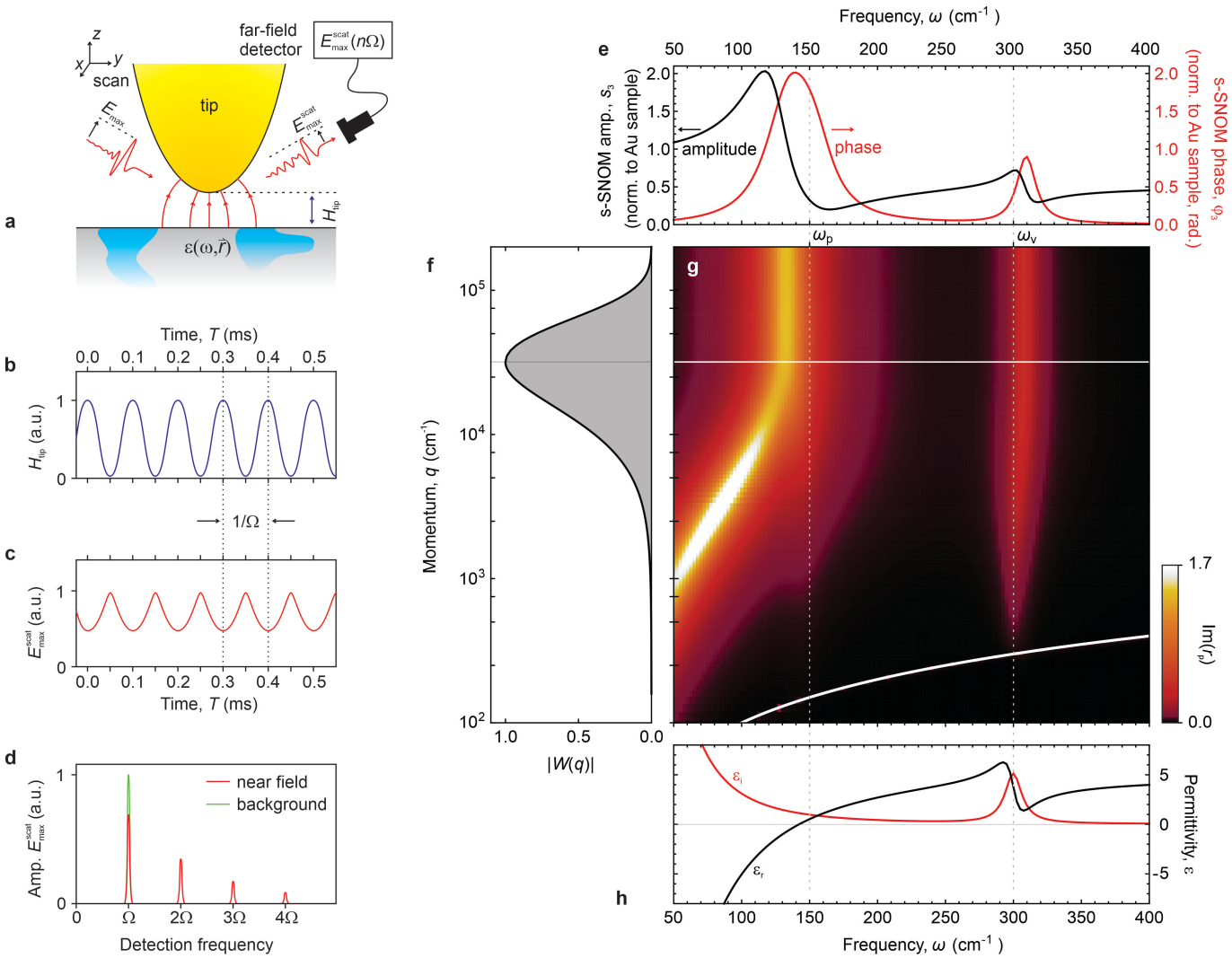
far-field detector
$E_{max}^{scat}(n\Omega)$
scan
tip
E_{max}
E_{max}^{scat}
H_{tip}
$\varepsilon(\omega,\vec{r})$
a
Time, T (ms)
b
H_{tip} (a.u.)
1/Ω
c
E_{max}^{scat} (a.u.)
Time, T (ms)
d
Amp. E_{max}^{scat} (a.u.)
near field
background
Detection frequency
Frequency, ω (cm^{-1})
e
s-SNOM amp., s_3 (norm. to Au sample)
s-SNOM phase, φ_3 (norm. to Au sample, rad.)
amplitude
phase
ω_p
ω_v
f
Momentum, q (cm^{-1})
$|W(q)|$
g
Im(r_p)
h
ε_i
ε_r
Permittivity, ε

388

Box 1 | Operational concept of scattering-type scanning near-field optical microscopy (s-SNOM) at terahertz frequencies. *Terahertz radiation with peak electric field E_{max} is focused onto a metallic scanning probe microscope tip (**a**). The radiation can be pulsed, as shown here, or continuous. Due to the lightning rod [38] and antenna [35,39] effects, it is concentrated to a nanoscale near-field spot at the tip apex. The near fields interact with the sample and act back upon the tip (indicated by red field lines in **a**), subsequently modifying the tip's polarization and the peak tip-scattered field E_{max}^{scat}. Recording the scattered spectral amplitude and phase with a far-field detector while scanning the sample position allows the sample's local complex dielectric function, $\varepsilon(\omega)$, to be mapped as a function of position, $\vec{r}$, on the nanoscale. The tip-scattered field also contains a large background contribution, e.g. scattering from the tip shaft and sample roughness, but this background can be effectively suppressed by combining amplitude- and phase-resolved detection with a demodulation technique [31,48]. The former can be achieved for continuous terahertz radiation with interferometric schemes or for pulsed terahertz radiation with electro-optic sampling, while the latter is typically based on sinusoidal modulation of the tip-sample distance, H_{tip}, as a function of time, T (**b**). Because the near-field interaction increases nonlinearly with decreasing H_{tip}, the associated tip-scattered near field is modulated anharmonically with T (**c**), whereas the tip-scattered background field is modulated harmonically. The pure near-field contribution to E_{max}^{scat} can thus be obtained by demodulating the detector signal at higher harmonics, n, of the tip's oscillation frequency, Ω, where n > 1 (**d**). Although other approaches have been established [36], the demodulation strategy has so far been the most efficient and practical method for background-free terahertz nanoimaging and spectroscopy based on elastic scattering at sharp metal tips.*

*The tip-sample near-field response (**e**) is governed by the momentum distribution of the reflected near fields – often referred to as the coupling weight function [53,75], $|W(q)|$ – and the frequency- and momentum-dependent Fresnel reflection coefficient of the sample, $r_p(\omega,q)$, where ω is the angular terahertz frequency and q is the in-plane momentum. For illustration of the resulting near-field spectroscopic contrasts, we approximate the near fields at the tip apex by those of a dipole located at the apex centre. With an apex of radius R = 50 nm located in contact with the sample, we obtain the coupling weight function shown in **f** with a maximum at approximately $q_{max} = 1/R$ [75]. For the sample, we consider a 100-nm-thick layer comprised of both mobile electrons (plasma frequency $\omega_p = 150\ cm^{-1}$) and a weak vibrational feature (resonance $\omega_v = 300\ cm^{-1}$). Describing the complex permittivity by the sum of Drude*

and Drude-Lorentz terms, we obtain the $\mathrm{Im}(r(\omega, q))$ *in* ***g****. The corresponding* $\varepsilon(\omega)$ *is shown in* ***h****. Notably, the tip probes the sample's reflection primarily at high-q values [53], yielding (after considering the multiple reflections between the tip and sample, i.e. the near-field interaction [11,30,31,40]) the* n^{th}*-order demodulated near-field amplitude* s_n *and phase* φ_n *spectra. Panel* ***e*** *shows the result for n=3 normalized to an Au sample, as is common for experimental measurements. Weak oscillators, such as the vibrational resonance at 300* cm^{-1}*, yield* s_n *and* φ_n *spectra that resemble the real and imaginary parts of* $\varepsilon(\omega)$*, respectively [76]. For negative sample permittivities (strong oscillators), the tip's near fields can resonantly excite localized surface polariton resonances, yielding large peaks in the* s_n *and* φ_n *spectra below* ω_p*, where* $\varepsilon_r(\omega)$ *is close to -1 [32,33]. Close to sample edges, terahertz s-SNOM can also map polaritons propagating along the sample surface (Fig. 3d). They are launched by the tip, reflected back by the sample edge, and interfere with the near field at the tip apex [66-68]. Constructive and destructive interference of the polaritons modify the effective tip illumination and thus the tip-scattered field, yielding fringe patterns, where the fringe spacing is half the polariton wavelength. In the example discussed in* ***g****, propagating surface plasmon polaritons exist for frequencies where* $\varepsilon_r(\omega) < -1$.

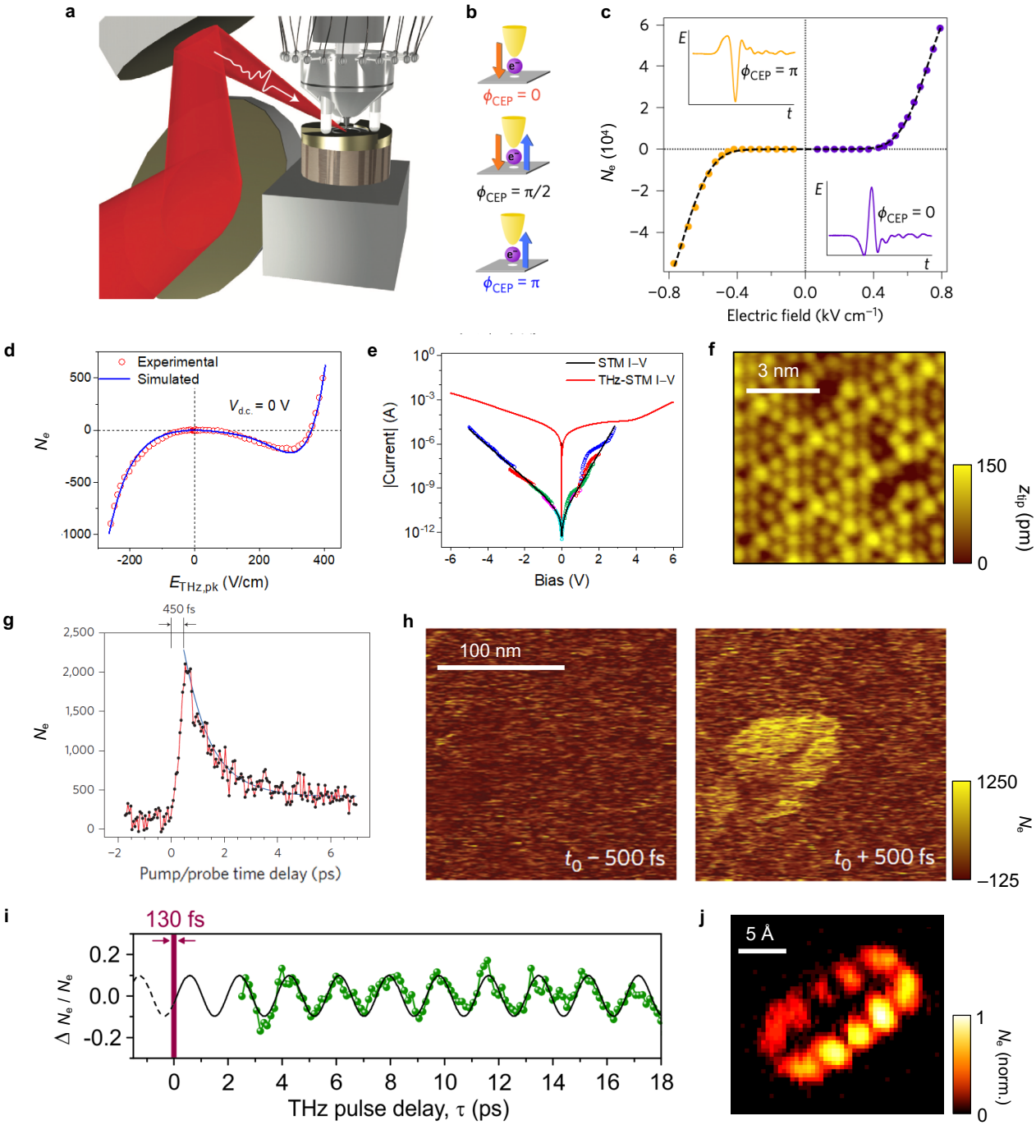
a
b
$\phi_{CEP} = 0$
$\phi_{CEP} = \pi/2$
$\phi_{CEP} = \pi$
c
N_e (10^4)
Electric field (kV cm^{-1})
$\phi_{CEP} = \pi$
$\phi_{CEP} = 0$
d
Experimental
Simulated
$V_{d.c.} = 0$ V
N_e
$E_{THz,pk}$ (V/cm)
e
STM I–V
THz-STM I–V
|Current| (A)
Bias (V)
f
3 nm
150
0
z_{tip} (pm)
g
450 fs
N_e
Pump/probe time delay (ps)
h
100 nm
$t_0 - 500$ fs
$t_0 + 500$ fs
1250
–125
N_e
i
130 fs
$\Delta N_e / N_e$
THz pulse delay, τ (ps)
j
5 Å
1
0
N_e (norm.)

429

Figure 4 | Ultrafast THz-STM imaging at nano and atomic scales. a, *In THz-STM, single-cycle, phase-stable terahertz pulses are focused onto the tip of a scanning tunneling microscope with polarization parallel to the tip axis.* ***b****, The THz-STM current is generated through terahertz coherent control of the tunnel junction resistance, so adjusting the temporal shape of the terahertz waveform, e.g. by changing the carrier envelope phase offset* ϕ_{CEP}*, modifies the average number of rectified elementary charges per terahertz pulse,* N_e*.* ***c****, If terahertz pulses with* $\phi_{CEP} = 0$ *(*$\phi_{CEP} = \pi$*) are defined as being cosine-like with a positive (negative) main peak, sweeping the terahertz peak field strength and recording* N_e *is analogous to a scanning tunneling spectroscopy (STS) measurement in conventional STM, albeit with further modelling required to extract the current-voltage (I-V) characteristic sampled by the terahertz pulse. In practice,* N_e *is measured as an average current,* $I_{THz} = e \times N_e \times f_{rep}$*, and calibrated based on the repetition rate of the laser,* f_{rep}*, and the elementary charge,* $e = 1.602 \times 10^{-19}$ *C.* ***d,*** N_e–$E_{THz,pk}$ *curve acquired on the Si(111)-(7×7) surface.* ***e,*** *Corresponding I–V curves for STM (black) and THz-STM (red) based on a simultaneous global fit of multiple data sets.* ***f,*** *Topographic image of the Si(111)-(7×7) surface, where the STM feedback loop maintains a constant terahertz-pulse-induced current with no d.c. bias present; image size 8.5 nm × 8.5 nm.* ***g,*** *Spatially localized optical-pump / THz-STM probe measurement at the center of a 60-nm-wide InAs nanodot.* ***h****, Ultrafast THz-STM snapshot images of an InAs nanodot acquired with the terahertz pulse arriving 500 fs before photoexcitation (left) and 500 fs after photoexcitation (right).* ***i,*** *THz-STM pump / THz-STM probe measurement of a pentacene molecule adsorbed on NaCl/Au(110) showing oscillations of the molecular frame relative to the substrate stimulated by terahertz-induced tunneling.* ***j,*** *THz-STM image of the highest occupied molecular orbital (HOMO) of a pentacene molecule. We note here that* I_{THz} *has often been used in the literature (including by the authors of this Review) to denote the number of rectified elementary charges per terahertz pulse, but this quantity would be better described as* N_e*, as outlined in Box 2. We have updated the axes here for consistency with this nomenclature. Adapted from:* ***a****, ref. [77];* ***b****,****c****, ref. [79];* ***d–f,*** *ref. [85];* ***g,h,*** *ref. [77];* ***i,j,*** *ref. [80].*

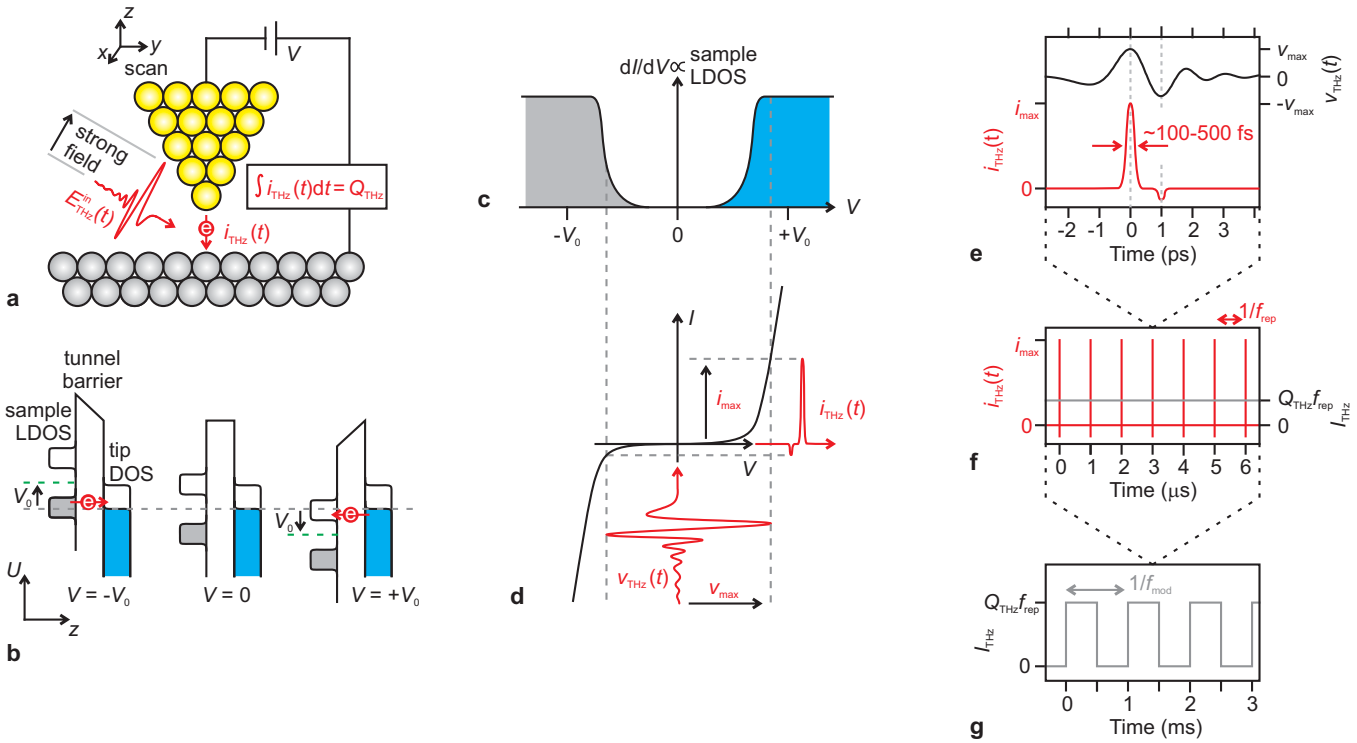
z
x
y
scan
V
strong field
$E^{in}_{THz}(t)$
$\int i_{THz}(t)dt = Q_{THz}$
$i_{THz}(t)$
a
tunnel barrier
sample LDOS
tip DOS
V_0
U
z
V = -V0
V = 0
V = +V0
b
dI/dV∝ sample LDOS
c
-V0
0
+V0
V
I
i_{max}
$i_{THz}(t)$
V
$v_{THz}(t)$
v_{max}
d
v_{max}
0
$-v_{max}$
$v_{THz}(t)$
i_{max}
$i_{THz}(t)$
~100-500 fs
0
-2 -1 0 1 2 3
Time (ps)
e
$1/f_{rep}$
i_{max}
$i_{THz}(t)$
0
$Q_{THz}f_{rep}$
0
I_{THz}
0 1 2 3 4 5 6
Time (μs)
f
$1/f_{mod}$
$Q_{THz}f_{rep}$
I_{THz}
0
0 1 2 3
Time (ms)
g

455

Box 2 | Operational concept of ultrafast lightwave-driven terahertz scanning tunnelling microscopy (THz-STM).

*A single-cycle, phase-stable terahertz pulse is coupled into a scanning tunnelling microscope tip-sample junction (**a**). The tip acts as a highly efficient antenna, such that the evanescent terahertz field at the tip apex is 10^5– 10^6 times enhanced compared to the incident field [77,79-83,85-90,92-94]. This increases the relatively modest incident terahertz field strength (~0.1 kV/cm) to the scale of interatomic fields in solids (>10 MV/cm = 1 V/nm). As a result, the terahertz field applied across the tip-sample junction, $E^{in}_{THz}(t)$, reaches the strong-field regime of nonlinear optics, where the oscillating electric field of a light pulse can be thought of as a quasi-static field [3,78] that adiabatically modifies the energy landscape. In the context of an STM junction, the terahertz field behaves as a quasi-static bias, $v_{THz}(t)$, and generates an ultrafast time-dependent tunnel current, $i_{THz}(t)$. Due to the bandwidth limitations of the STM electronics, only the temporal integral of this current response, Q_{THz}, can be measured. In general, we use lowercase notation here to denote time-dependent quantities associated with coherent terahertz control of the tunnel junction and uppercase notation to denote the steady-state voltage (V) and current (I) that can be applied and measured by conventional STM, respectively. **b**, A static bias applied to the tunnel junction shifts the Fermi level of the sample (green dashed line) relative to that of the tip (grey dashed line), such that a net current flows through the tunnel barrier. This is visualized in the schematic as electron flow between the density of states (DOS) of the tip and the local DOS of the sample (LDOS), where the precise sample LDOS is determined by the tip position and U represents energy. A semiconducting sample is selected as an example, with a filled valence band (grey shaded region below the sample's Fermi level) and an empty conduction band (unshaded region above the sample's Fermi level). We ignore band bending in this simple schematic [84,85]. The tip is metallic, with electrons filled to its Fermi level (blue shaded region below tip's Fermi level). In this situation, a net current is present only when the filled states of the valence band align with the empty states of the tip (e.g. $V = -V_o$, left) or the empty states of the conduction band align with the filled states of the tip (e.g. $V = +V_o$, right). Within the quasi-static approximation of THz-STM, the terahertz voltage at time t defines the instantaneous state of the tunnel junction, such that the terahertz voltage transient sweeps the system through a series of configurations such as those shown in the schematic. **c**, A conventional scanning tunnelling spectroscopy (STS) experiment reveals the differential conductance (dI/dV) of the junction, which is proportional to the LDOS of the sample, e.g. the semiconductor shown in (**b**). **d**, Features in the*

LDOS correspond to nonlinearities in the current-voltage (I-V) characteristic of the junction. These nonlinearities are the key to THz-STM, where the terahertz-induced current must be asymmetric in order to yield a measurable Q_{THz}*. In practice, the terahertz voltage pulse is rectified by a nonlinear I-V characteristic, with the symmetry of the terahertz pulse, the symmetry of the I-V characteristic, and the static bias voltage determining the precise THz-STM signal (**d**). The full width at half maximum (FWHM) of the main peak of* $i_{THz}(t)$ *is sub-cycle on the terahertz oscillation timescale due to the nonlinear generation process (**e**). Current pulses with FWHM of 100 fs - 500 fs have been observed experimentally [77,80,81,85,86,88,89]. The terahertz pulse focused onto the tip is part of a pulse train since it is generated by a train of ultrafast near-infrared pulses from a laser amplifier (**f**). Therefore, a train of current pulses is produced that is separated by the inverse of the repetition rate,* $1/f_{rep}$*. Optimized signal-to-noise ratios are achieved for repetition rates >100 kHz, which is above the typical bandwidth of an STM preamplifier. The terahertz-induced current that is actually measured is thus a d.c. current,* $I_{THz} = Q_{THz} f_{rep}$*, which adds to the normal d.c. tunnel current. It is typically reported as the net number of elementary charges rectified by each terahertz pulse on average, defined here as* $N_e = Q_{THz} / e$*, where* $e = 1.602 \times 10^{-19}$ *C. To isolate* I_{THz} *from the normal tunnel current and improve the detection signal-to-noise ratio the THz pulse train is modulated (**g**) at a frequency,* f_{mod}*, within the bandwidth of the preamplifier but above the bandwidth of the STM feedback loop. The second condition prevents the tip height from oscillating when operating in constant current mode but can be relaxed when measurements are taken in constant height mode. Conversely, in terahertz-driven mode, where no d.c. bias is present and the feedback responds only to the terahertz-driven current, chopping is unnecessary [85,86].*

Acknowledgements

The authors thank Lars Mester (CIC nanoGUNE) for the preparation of panel **e** of Box 1.

T.L.C. acknowledges financial support from the Office of Naval Research (Grant no. N00014-19-1-2051) and the Cowen Family Endowment.

R.H. acknowledges financial support from the Spanish Ministry of Science, Innovation and Universities (national project RTI2018-094830-B-100 and the project MDM-2016-0618 of the Marie de Maeztu Units of Excellence Program) and the Basque Government (grant No. IT1164-19).

F.A.H. acknowledges support from the Natural Sciences and Engineering Research Council of Canada (NSERC), the Canada Foundation for Innovation (CFI), and the Alberta Innovates Technology Futures (AITF) Strategic Chairs Program.

Competing interests

R.H. is a co-founder of Neaspec GmbH, a company producing scattering-type scanning near-field optical microscope systems, such as the ones described in this review. The remaining authors declare no competing interests.

References

1. Jepsen, P. U., Cooke, D. G. & Koch, M. Terahertz spectroscopy and imaging—modern techniques and applications. *Laser Photon. Rev.* **5,** 124–166 (2011).
2. Ulbricht, R., Hendry, E., Shan, J., Heinz, T. F. & Bonn, M. Carrier dynamics in semiconductors studied with time-resolved terahertz spectroscopy. *Rev. Mod. Phys.* **83,** 543–586 (2011).
3. Kampfrath, T., Tanaka, K. & Nelson, K. A. Resonant and nonresonant control over matter and light by intense terahertz transients. *Nat. Photon.* **7,** 680–690 (2013).
4. Joyce, H. J., Boland, J. L., Davies, C. L., Baig, S. A. & Johnston, M. B. A review of the electrical properties of semiconductor nanowires: insights gained from terahertz conductivity spectroscopy. *Semicond. Sci. Technol.* **31**, 103003 (2016).
5. Dhillon, S. S. *et al.* The 2017 terahertz science and technology roadmap. *J. Phys. D: Appl. Phys.* **50,** 043001 (2017).
6. Spies, J. A., Neu, J., Tayvah, U. T., Capobianco, M. D., Pattengale, B., Ostresh, S. & Schmuttenmaer, C. A. Terahertz Spectroscopy of Emerging Materials. *J. Phys. Chem. C* **124**, 22335 (2020).
7. Ponseca, Jr., C. S., Chábera, P., Uhlig, J., Persson, P. & Sundström, V. Ultrafast Electron Dynamics in Solar Energy Conversion. *Chem. Rev.* **117**, 10940-11024 (2017).
8. Lan, Y., Dringoli, B. J., Valverde-Chávez, D. A., Ponseca, Jr., C. S., Sutton, M., He, Y., Kanatzidis, M. G. & Cooke, D. G. Ultrafast correlated charge and lattice motion in a hybrid metal halide perovskite. *Sci. Adv.* **5**, eaaw5558 (2019).
9. Kužel, P. & Němec, H. Terahertz conductivity in nanoscaled systems: effective medium theory aspects. *J. Phys. D: Appl. Phys.* **47**, 374005 (2014).
10. Cocker, T. L., Baillie, D., Buruma, M., Titova, L. V., Sydora, R. D., Marsiglio, F. & Hegmann, F. A. Microscopic origin of the Drude-Smith model. *Phys. Rev. B* **96**, 205349 (2017).
11. Keilmann, F. & Hillenbrand, R. Near-field microscopy by elastic light scattering from a tip. *Phil. Trans. R. Soc. Lond. A* **362,** 787–805 (2004).
12. Novotny, L. Chapter 5 The history of near-field optics. *Prog. Optics* **50**, 137 (2007).
13. Chen, X., Hu, D., Mescall, R., You, G., Basov, D. N., Dai, Q. & Liu, M. Modern scattering-type scanning near-field optical microscopy for advanced material research. *Adv. Mater.* **31,** 1804774 (2019).
14. Keiser, G. R. & Klarskov, P. Terahertz Field Confinement in Nonlinear Metamaterials and Near-Field Imaging. *Photonics* **6**, 22 (2019).
15. Kiwa, T., Tonouchi, M., Yamashita, M. & Kawase, K. Laser terahertz-emission microscope for inspecting electrical faults in integrated circuits. *Opt. Lett.* **28,** 2058–2060 (2003).
16. van der Valk, N. C. J. & Planken, P. C. M. Electro-optic detection of subwavelength terahertz spot sizes in the near field of a metal tip. *Appl. Phys. Lett.* **81**, 1558 (2002).
17. Adam, A. J. L., Brok, J. M., Seo, M. A., Ahn, K. J., Kim, D. S., Kang, J. H., Park, Q. H., Nagel, M. & Planken, P. C. M. Advanced terahertz electric near-field measurements at sub-wavelength diameter metallic apertures. *Opt. Express* **16,** 7407–7407 (2008).
18. Blanchard, F. & Tanaka, K. Improving time and space resolution in electro-optic sampling for near-field terahertz imaging. *Opt. Lett.* **41,** 4645–4648 (2016).
19. Knab, J. R., Adam, A. J. L., Shaner, E., Starmans, H. J. A. J. & Planken, P. C. M. Terahertz near-field spectroscopy of filled subwavelength sized apertures in thin metal films. *Opt. Express* **21**, 1101 (2013).
20. Niessen, K. A., Xu, M., George, D. K., Chen, M. C., Ferré-D'Amaré, A. R., Snell, E. H., Cody, V., Pace, J., Schmidt, M. & Markelz, A. G. Protein and RNA dynamical fingerprinting. *Nat. Commun.* **10**, 1026 (2019).
21. Mitrofanov, O., Lee, M., Hsu, J. W. P., Pfeiffer, L. N., West, K. W., Wynn, J. D. & Federici, J. F. Terahertz pulse propagation through small apertures. *Appl. Phys. Lett.* **79,** 907–909 (2001).
22. Macfaden, A. J., Reno, J. L., Brener, I. & Mitrofanov, O. 3 μm aperture probes for near-field terahertz transmission microscopy. *Appl. Phys. Lett.* **104**, 011110 (2014).
23. Kawano, Y. & Ishibashi, K. An on-chip near-field terahertz probe and detector. *Nat. Photon.* **2,** 618–621 (2008).

24. Mitrofanov, O., Viti, L., Dardanis, E., Giordano, M. C., Ercolani, D., Politano, A., Sorba, L. & Vitiello, M. Near-field terahertz probes with room-temperature nanodetectors for subwavelength resolution imaging. *Sci. Rep.* **7**, 44240 (2017).
25. Wächter, M. Nagel, M. & Kurz, H. Tapered photoconductive terahertz field probe tip with subwavelength spatial resolution. *Appl. Phys. Lett.* **95,** 041112 (2009).
26. Bhattacherya, A. & Gómez Rivas J. Full vectorial mapping of the complex electric near-fields of THz resonators. *APL Photonics* **1**, 086103 (2016).
27. Kawata, S. & Inouye, Y. Scanning probe optical microscopy using a metallic probe tip. *Ultramicroscopy* **57**, 313 (1995).
28. Zenhausern, F., Martin, Y. & Wickramasinghe, H. K. Scanning Interferometric Apertureless Microscopy: Optical Imaging at 10 Angstrom Resolution. *Science* **269**, 1083 (1995).
29. Lahrech, A., Bachelot, R., Gleyzes, P. & Boccara, A. C. Infrared-reflection-mode near-field microscopy using an apertureless probe with resolution of λ/600. *Opt. Lett.* **21**, 1315 (1996).
30. Knoll, B. & Keilmann, F. Near-field probing of vibrational absorption for chemical microscopy. *Nature* **399**, 134 (1999).
31. Hillenbrand, R. & Keilmann, F. Complex optical constants on a subwavelength scale. *Phys. Rev. Lett.* **85,** 3029–3032 (2000).
32. Knoll, B. & Keilmann, F. Infrared conductivity mapping for nanoelectronics. *Appl. Phys. Lett.* **77**, 2980 (2000).
33. Hillenbrand, R., Taubner, T. & Keilmann, F. Phonon-enhanced light–matter interaction at the nanometre scale. *Nature* **418,** 159–162 (2002).
34. Chen, H.-T., Kersting, R. & Cho, G. C. Terahertz imaging with nanometer resolution. *Appl. Phys. Lett.* **83,** 3009–3011 (2003).
35. Wang, K., Mittleman, D. M., van der Valk, N. C. J. & Planken, P. C. M. Antenna effects in terahertz apertureless near-field optical microscopy. *Appl. Phys. Lett.* **85,** 2715–2717 (2004).
36. Buersgens, F., Kersting, R. & Chen, H.-T. Terahertz microscopy of charge carriers in semiconductors. *Appl. Phys. Lett.* **88,** 112115 (2006).
37. von Ribbeck, H.-G., Brehm, M., van der Weide, D., Winnerl, S., Drachenko, O., Helm, M. & Keilmann, F. Spectroscopic THz near-field microscope. *Opt. Express* **16,** 3430–3438 (2008).
38. Huber, A. J., Keilmann, F.,Wittborn, J., Aizpurua, J. & Hillenbrand, R. Terahertz near-field nanoscopy of mobile carriers in single semiconductor nanodevices. *Nano Lett.* **8,** 3766–3770 (2008).
39. Mastel, S., Lundeberg, M. B., Alonso-González, P., Gao, Y., Watanbe, K., Taniguchi, T., Hone, J., Koppens, F. H. L., Nikitin, A. Y. & Hillenbrand, R. Terahertz nanofocusing with cantilevered terahertz-resonant antenna tips. *Nano Lett.* **17,** 6526–6533 (2017).
40. Maissen, C., Chen, S., Nikulina, E., Govyadinov, A. & Hillenbrand, R. Probes for ultrasensitive THz nanoscopy. *ACS Photon.* **6,** 1279–1288 (2019).
41. Siday, T., Hale, L. L., Hermans, R. I. and Mitrofanov, O. Resonance-Enhanced Terahertz Nanoscopy Probes. *ACS Photon*. **7**, 596 (2020).42.Chen, C., Chen, S., Lobo, R. P. S. M., Maciel-Escudero, C., Lewin, M., Taubner, T., Xiong, W., Xu, M., Zhang, X., Miao, X., Li, P. & Hillenbrand, R. Terahertz Nanoimaging and Nanospectroscopy of Chalcogenide Phase-Change Materials. *ACS Photon*. **7**, 3499-3506 (2020).
43. Giordano, M. C., Mastel, S., Liewald, C., Columbo, L. L., Brambilla, M., Viti, L., Politano, A., Zhang, K., Li, L., Davies, A. G., Linfield, E. H., Hillenbrand, R., Keilmann, F., Scamarcio, G. & Vitiello, M. Phase-resolved terahertz self-detection near-field microscopy. *Opt. Express* **26**, 18423 (2018).
44. Jacob, R., Winnerl, S., Fehrenbacher, M., Bhattacharyya, J., Schneider, H., Wenzel, M. T., von Ribbeck, H.-G., Eng, L. M., Atkinson, P., Schmidt, O. G. & Helm, M. Intersublevel spectroscopy on single InAs-quantum dots by terahertz near-field microscopy. *Nano Lett.* **12,** 4336–4340 (2012).
45. Kuschewski, F., von Ribbeck, H.-G., Döring, J., Winnerl, S., Eng, L. M. & Kehr, S. C. Narrow-band near-field nanoscopy in the spectral range from 1.3 to 8.5 THz. *Appl. Phys. Lett.* **108,** 113102 (2016).
46. Liewald, C., Mastel, S., Hesler, J., Huber, A. J., Hillenbrand, R. & Keilmann, F. All-electronic terahertz nanoscopy. *Optica* **5,** 159–162 (2018).

47. Chen, X., Liu, X., Guo, X., Chen, S., Hu, H., Nikulina, E., Ye, X., Yao, Z., Bechtel, H. A., Martin, M. C., Carr, G. L., Dai, Q., Zhuang, S., Hu, Q., Zhu, Y., Hillenbrand, R., Liu, M. & You, G. THz Near-Field Imaging of Extreme Subwavelength Metal Structures. *ACS Photon.* **7**, 687-694 (2020).
48. Ocelic, N., Huber, A. & Hillenbrand, R. Pseudoheterodyne detection for background-free near-field spectroscopy. *Appl. Phys. Lett.* **89**, 101124 (2006).
49. Huth, F., Schnell, M., Wittborn, J., Ocelic, N. & Hillenbrand, R. Infrared-spectroscopic nanoimaging with a thermal source. *Nature Mater.* **10,** 352–355 (2011).
50. Khatib, O., Bechtel, H. A., Martin, M. C., Raschke, M. B. and Carr, G. L. Far Infrared Synchrotron Near-Field Nanoimaging and Nanospectroscopy. *ACS Photon*. **5**, 2773 (2018).
51. Moon, K., Park, H., Kim, J., Do, Y., Lee, S., Lee, G., Kang, H. & Han, H. Subsurface nanoimaging by broadband terahertz pulse nearfield microscopy. *Nano Lett.* **15,** 549–552 (2014).
52. Stinson, H. T. *et al.* Imaging the nanoscale phase separation in vanadium dioxide thin films at terahertz frequencies. *Nat. Commun.* **9,** 3604 (2018).
53. Zhang, J., Chen, X., Mills, S., Ciavatti, T., Yao, Z., Mescall, R., Hu, H., Semenenko, V., Fei, Z., Li, H., Perebeinos, V., Tao, H., Dai, Q., Du, X. & Liu, M. Terahertz Nanoimaging of Graphene. *ACS Photon.* **5**, 2645 (2018).
54. Aghamiri, N. A., Huth, F., Huber, A. J., Fali, A., Hillenbrand, R. & Abate, Y. Hyperspectral time-domain terahertz nanoimaging. *Opt. Express* **27,** 24231–24242 (2019).
55. Moon, K., Do, Y., Park, H., Kim, J., Kang, H., Lee, G., Lim, J.-H., Kim, J.-W., Han, H. Computed terahertz near-field mapping of molecular resonances of lactose stereo-isomer impurities with sub-attomole sensitivity. *Sci*. *Adv*. **9**, 16915 (2019).
56. Eisele, M., Cocker, T. L., Huber, M. A., Plankl, M., Viti, L., Ercolani, D., Sorba, L., Vitiello, M. S. & Huber, R. Ultrafast multi-terahertz nano-spectroscopy with sub-cycle temporal resolution. *Nat. Photon.* **8,** 841–845 (2014).
57. Wagner, M., McLeod, A. S., Maddox, S. J., Fei, Z., Liu, M., Averitt, R. D., Fogler, M. M., Bank, S. R., Keilmann, F. & Basov, D. N. Ultrafast Dynamics of Surface Plasmons in InAs by Time-Resolved Intrared Nanospectroscopy. *Nano Lett*. **14**, 4529 (2014).
58. Yao, Z., Semenenko, V., Zhang, J., Mills, S., Zhao, X., Chen, X., Hu, H., Mescall, R., Ciavatti, T., March, S., Bank, S. R., Tao, T. H., Zhang, X., Perebeinos, V., Dai, Q., Du, X. & Liu, M. Photo-induced terahertz near-field dynamics of graphene/InAs heterostructures. *Opt. Express* **27,** 13611–13623 (2019).
59. Yang, H. U., Hebestreit, E., Josberger, E. E. & Raschke, M. B. A cryogenic scattering-type scanning near-field optical microscope. *Rev. Sci. Instrum.* **84**, 023701 (2013).
60. McLeod, A. S., van Heumen, E., Ramirez, J. G., Wang, S., Saerbeck, T., Guenon, S., Goldflam, M., Anderegg, L., Kelly, P., Mueller, A., Liu, M. K., Schuller, I. K. & Basov, D. N. Nanotextured phase coexistence in the correlated insulator V_2O_3. *Nat. Phys.* **13,** 80–86 (2016).
61. Lang, D., Döring, J., Nörenberg, T., Butykai, A., Kézsmárki, I., Schneider, H., Winnerl, S., Helm, M., Kehr, S. C. and Eng, L. M. Infrared nanoscopy down to liquid helium temperatures. *Rev. Sci. Instrum*. **89**, 033702 (2018).
62. Weng, Q., Komiyama, S., Yang, L., An, Z., Chen, P., Biehs, S.-A., Kajihara, Y. & Lu, W. Imaging of nonlocal hot-electron energy dissipation via shot noise. *Science* **360,** 775–778 (2018).
63. de Wilde, Y., Formanek, F., Carminati, R., Gralak, B., Lemoine, P.-A., Joulain, K., Mulet, J.-P., Chen, Y. and Greffet, J.-J. Thermal radiation scanning tunnelling microscopy. *Nature* **444**, 740 (2006).
64. Komiyama, S. Perspective: Nanoscopy of charge kinetics via terahertz fluctuation. *J. Appl. Phys.***125**, 010901 (2019).
65. Lin, K.-T., Komiyama, S., Kim, S., Kawamura, K. & Kajihara, Y. A high signal-to-noise ratio passive near-field microscope equipped with a helium-free cryostat. *Rev. Sci. Instrum.* **88,** 013706 (2017).
66. Chen, J. *et al.* Optical nano-imaging of gate-tunable graphene plasmons. *Nature* **487,** 77–81 (2012).
67. Fei, Z. *et al.* Gate-tuning of graphene plasmons revealed by infrared nano-imaging. *Nature* **487,** 82–82 (2012).
68. de Oliveira, T. V. A. G., Nörenberg, T., Álvarez-Pérez, G., Wehmeier, L., Taboada-Gutiérrez, J., Obst, M., Hempel, F., Lee, E. J. H., Klopf, J. M., Errea, I., Nikitin, A. Y., Kehr, S. C., Alonso-Gonzaléz and Eng, L. M. Nanoscale-Confined Terahertz Polaritons in a van der Waals Crystal. *Adv. Mater.* **33**, 2005777 (2021).

69. Alonso-González, P., Nikitin, A. Y., Gao, Y., Woessner, A., Lundeberg, M. B., Principi, A., Forcellini, N., Yan, W., Vélez, S., Huber, A. J., Watanabe, K., Taniguchi, T., Casanova, F., Hueso, L. E., Polini, M., Hone, J., Koppens, F. H. L. & Hillenbrand, R. Acoustic terahertz graphene plasmons revealed by photocurrent nanoscopy. *Nat. Nanotech.* **12,** 31–35 (2017).
70. Lundeberg, M. B. *et al.* Tuning quantum nonlocal effects in graphene plasmonics. *Science* **357,** 187–191 (2017).
71. Klarskov, P., Kim, H., Colvin, V. L. & Mittleman, D. M. Nanoscale laser terahertz emission microscopy. *ACS Photonics* **4,** 2676–2680 (2017).
72. Pizzuto, A., Mittleman, D. M. & Klarskov, P. Laser THz emission nanoscopy THz nanoscopy. *Opt. Express* **28,** 18778 (2020).
73. Schumacher, Z., Rejali, R., Pachlatko, R., Spielhofer, A., Nagler, P., Miyahara, T. Cooke, D. G. & Grütter, P. Nanoscale force sensing of an ultrafast nonlinear optical response. *Proc. Nal. Acad. Sci.* **117,** 19773–19779 (2020).
74. Qazilbash, M. M. *et al.* Mott transition in VO_2 revealed by infrared spectroscopy and nano-imaging. *Science* **318,** 1750–1753 (2007).
75. Fei, Z. *et al*. Infrared Nanoscopy of Dirac Plasmons at the Graphene – SiO_2 Interface. *Nano Lett*. **11**, 4701 (2011).
76. Taubner, T., Hillenbrand, R. and Keilmann, F. Nanoscale polymer recognition by spectral signature in scattering infrared near-field microscopy. *Appl. Phys. Lett.* **85**, 5064 (2004).
77. Cocker, T. L., Jelic, V., Gupta, M., Molesky, S. J., Burgess, J. A. J., Reyes, G. D. L., Titova, L. V., Tsui, Y. Y., Freeman, M. R. & Hegmann, F. A. An ultrafast terahertz scanning tunnelling microscope. *Nature Photon.* **7,** 620–625 (2013).
78. Keldysh, L. V. Ionization in the field of a strong electromagnetic wave *Sov. Phys. JETP* **20,** 1307–1314 (1965).
79. Yoshioka, K., Katayama, I., Minami, Y., Kitajima, M., Yoshida, S., Shigekawa, H. & Takeda, J. Real-space coherent manipulation of electrons in a single tunnel junction by single-cycle terahertz electric fields. *Nat. Photon.* **10,** 762–765 (2016).
80. Cocker, T. L., Peller, D., Yu, P., Repp, J. & Huber, R. Tracking the ultrafast motion of a single molecule by femtosecond orbital imaging. *Nature* **539,** 263–267 (2016).
81. Yoshida, S., Hirori, H., Tachizaki, T., Yoshioka, K., Arashida, Y., Wang, Z.-H., Sanari, Y., Takeuchi, O., Kanemitsu, Y. & Shigekawa, H. Subcycle transient scanning tunneling spectroscopy with visualization of enhanced terahertz near field. *ACS Photon.* **6,** 1356–1364 (2019).
82. Peller, D., Kastner, L. Z., Buchner, T. Roelcke, C., Albrecht, F., Moll, N., Huber, R. and Repp, J. Sub-cycle atomic-scale forces coherently control a single-molecule switch. *Nature* **585**, 58 (2020).
83. Tian, Y., Yang, F., Guo, C. & Jiang, Y. Recent Advances in Ultrafast Time-Resolved Scanning Tunneling Microscopy. *Surf. Rev. Lett.* **25**, 1841003 (2018).
84. Chen, C. J. Introduction to Scanning Tunneling Microscopy 2nd Edition (Oxford University Press, 2008).
85. Jelic, V., Iwaszczuk, K., Nguyen, P. H., Rathje, C., Hornig, G. J., Sharum, H. M., Hoffman, J. R., Freeman, M. R. & Hegmann, F. A. Ultrafast terahertz control of extreme tunnel currents through single atoms on a silicon surface. *Nat. Phys.* **13,** 591–598 (2017).
86. Luo, Y., Jelic, V., Chen, G., Nguyen, P. H., Liu, Y.-J. R., Calzada, J. A. M., Mildenberger, D. J. and Hegmann, F. A. Nanoscale terahertz STM imaging of a metal surface. *Phys. Rev. B* **102**, 205417 (2020).
87. Nguyen, P. H., Rathje, C., Hornig, G. J., Jelic, V., Ropers, C. and Hegmann, F. A. Coupling Terahertz Pulses to a Scanning Tunneling Microscope. *Phys. In Canada* **71**, 157 (2015).
88. Yoshioka, K., Katayama, I., Arashida, Y., Ban, A., Kawada, Y., Konishi, K., Takahashi, H. & Takeda, J. Tailoring single-cycle near field in a tunnel junction with carrier-envelope phase-controlled terahertz electric fields. *Nano Lett.* **18,** 5198–5204 (2018).
89. Müller, M., Sabanés, N. M., Kampfrath, T. & Wolf., M. Phase-resolved detection of ultrabroadband THz pulses inside a scanning tunneling microscope junction. *ACS Photon.* **7,** 2046–2055 (2020).
90. Peller, D., Roelcke, C., Kastner, L. Z., Buchner, T., Neef, A., Hayes, J., Bonafé, F., Sidler, D., Ruggenthaler, M., Rubio, A., Huber, R. & Repp, J. Quantitative sampling of atomic-scale electromagnetic waveforms. *Nature Photon.* **15**, 143-147 (2021).

91. Wimmer, L., Herink, G., Solli, D. R., Yalunin, S. V., Echternkamp, K. E. & Ropers, C. Terahertz control of nanotip photoemission. *Nat. Phys.* **10,** 432–436 (2014).
92. Du, S., Yoshida, K., Zhang, Y., Hamada, I. & Hirakawa, K. Terahertz dynamics of electron-vibron coupling in single molecules with tunable electrostatic potential. *Nat. Photon.* **12,** 608–612 (2018).
93. Kang, T., Bahk, Y.-M. & Kim, D.-S. Terahertz quantum plasmonics at nanoscales and angstrom scales. *Nanophotonics* **9,** 435–451 (2020).
94. Lange, S. L., Noori, N. K., Kristensen, T. M. B., Steenberg, K. & Jepsen, P. U. Ultrafast THz-driven electron emission from metal metasurfaces. *J. Appl. Phys.* **128**, 070901 (2020).
95. Yarotski, D. A. *et al*. Ultrafast carrier-relaxation dynamics in self-assembled InAs/GaAs quantum dots. *J. Opt. Soc. Am. B* **19,** 1480–1484 (2002).
96. Shi, T., Cirac, J. I. & Demler, E. Ultrafast molecular dynamics in terahertz-STM experiments: Theoretical analysis using Anderson-Holstein model. *Phys. Rev. Res.* **2**, 033379 (2020).
97. Amenabar, I., Poly, S., Nuansing, W., Hubrich, E. H., Govyadinov, A. A., Huth, F., Krutokhvostov, R., Zhang, L., Knez, M., Heberle, J., Bittner, A. M. & Hillenbrand, R. Structural analysis and mapping of individual protein complexes by infrared nanospectroscopy. *Nat. Commun.* **4**, 2890 (2013).
98. Kravtsov, V., Ulbricht, R., Atkin, J. M. & Raschke, M. B. Plasmonc nanofocused four-wave mixing for femtosecond near-field imaging. *Nat. Nanotech.* **11,** 459–464 (2016).
99. Lang, D., Balaghi, L., Winnerl, S., Schneider, H., Hübner, R., Kehr, S. C., Eng, L. M., Helm, M., Dimakis, E. & Pashkin, A. Nonlinear plasmonic response of doped nanowires observed by infrared nanospectroscopy. *Nanotechnol*. **30**, 084003 (2019).
100. Kwok, Y., Chen, G. & Mukamel, S. STM imaging of electron migration in real space and time: a simulation study. *Nano Lett.* **19,** 7006–7012 (2019).
101. Frankerl, M. & Donarini, A. Spin-orbit interaction induces charge beatings in a lightwave-STM – single molecule junction. *Phys. Rev. B* **103**, 085420 (2021).
102. Yoshida, S., Arashida, Y., Hirori, H., Tachizaki, T., Taninaka, A., Ueno, H., Takeuchi, O. & Shigekawa, H. Terahertz Scanning Tunneling Microscopy for Visualizing Ultrafast Electron Motion in Nanoscale Potential Variations. *ACS Photon*. **8**, 315-323 (2021).
103. Kimura, K., Morinaga, Y., Imada, H., Katayama, I., Asakawa, K., Yoshioka, K., Kim, Y. & Takeda, J. Terahertz-Field-Driven Scanning Tunneling Luminescence Spectroscopy. *ACS Photon*. **XXXX**, XXXX-XXXX (2021).
104. Abdo, M., Sheng, S., Rolf-Pissarczyk, S., Arnhold, L., Burgess, J. A. J., Isobe, M., Malavolti, L. & Loth, S. Variable Repetition Rate THz Source for Ultrafast Scanning Tunneling Microscopy. *ACS Photon.* **8**, 702-708 (2021).
105. Peplow, M. The Next Big Hit in Molecule Hollywood. *Nature* **544**, 408-410 (2017).
106. Geaney, S., Cox, D., Hönigl-Decrinis, T., Shaikhaidarov, R., Kubatkin, S. E., Lindström, T., Danilov, A. V. and de Graaf, S. E. Near-Field Scanning Microwave Microscopy in the Single Photon Regime. *Sci. Rep.* **9**, 12539 (2019).
107. Li, S. & Jones, R. R. High-energy electron emission from metallic nanotips driven by intense single-cycle terahertz pulses. *Nat. Commun.* **7,** 13405 (2016).
108. Matte, D., Chamanara, N., Gingras, L., Cooke, D. G., René de Cotret, L. P., Britt, T. L. & Siwick, B. Extreme lightwave electron field emission from a nanotip. *Phys. Rev. Res.* **3**, 013137 (2021).
109. Völcker, M., Krieger,W. &Walther, H. Laser-driven scanning tunneling microscope. *Phys. Rev. Lett.* **66,** 1717–1720 (1991).
110. Rybka, T., Ludwig, M., Schmalz, M. F., Knittel, V., Brida, D. & Leitenstorfer, A. Sub-cycle optical phase control of nanotunnelling in the single-electron regime. *Nat. Photon.* **10,** 667–670 (2016).
111. Garg, M. & Kern, K. Attosecond coherent manipulation of electrons in tunnelling microscopy. *Science* **367,** 411–415 (2020).